Coastal Engineering 89 (2014) 99–105

Contents lists available at ScienceDirect

Coastal Engineering

journal homepage: www.elsevier.com/locate/coastaleng

Short communication

Sediment transport and morphodynamics generated by a dam-break swash uprush: Coupled vs uncoupled modeling

Matteo Postacchini [a,*], Ilya K. Othman [b], Maurizio Brocchini [a], Tom E. Baldock [c]

[a] Department of ICEA, Università Politecnica delle Marche, Ancona, Italy
[b] Faculty of Civil Engineering, Universiti Teknologi Malaysia, UTM Skudai, 81310 Johor, Malaysia
[c] Division of Civil Engineering, University of Queensland, Brisbane, QLD 4072, Australia

ARTICLE INFO

Article history:
Received 10 January 2014
Received in revised form 4 April 2014
Accepted 7 April 2014
Available online 4 May 2014

Keywords:
Sediment transport
Swash zone
Dam break
Laboratory experiments
Hydro-morphodynamic solver

ABSTRACT

The present work analyzes the hydro-morphodynamics characterizing the swash region during the uprush stage. A comparison is illustrated between the sediment transport measured in a series of dam-break experiments and that predicted by the numerical hydro-morphodynamic model of Postacchini et al. (2012). The primary aim is to investigate the differences arising between the weakly coupled or uncoupled model and the measurements, in terms of hydrodynamics, tip celerity and sediment transport. The hydrodynamics are well described by the model and results have been used to calibrate both friction factor and subgrid turbulent viscosity. Comparison of numerically-computed tip celerity with experimental data reveals a fairly good agreement, i.e. a mean error of about 10%, while modeled sediment transport differs by about 40% from the available data. No evident differences are found between results obtained from the coupled and uncoupled model runs (2% for the celerity and 11% for the sediment transport rate at the tip), suggesting that for the specific flow under investigation, at the leading edge of the swash front, hydro-morphological coupling is not an issue of fundamental importance. However, for the special case here of a swash forced by a dam-break, scour occurs at the dam location, and in this case the erosion of the bed is significantly larger in the uncoupled model.

1. Introduction

Because of the fundamental influence of the swash zone morphodynamics on the beach-face evolution (e.g. the cross-shore sediment exchange between subaerial and sub-aqueous zones, intense longshore sediment transport), much research is being devoted to this subject (e.g. Brocchini, 2013; Brocchini and Baldock, 2008; Elfrink and Baldock, 2002; Masselink and Puleo, 2006). Studies range from laboratory (e.g. Alsina et al., 2012; Baldock et al., 2011) to field (e.g. Aagaard and Hughes, 2006; Blenkinsopp et al., 2011; Masselink and Russel, 2006) experiments, with an increasing interest in the flexibility and power of numerical experiments (e.g. Bakhtyar et al., 2010). The usefulness of such numerical experiments is a function of a balance between suitable representation of the physics at hand and the computational costs entailed by the calculations. In this respect, depth-averaged solvers provide optimal performance and enable long-enough computations for morphological purposes, at least over short time-scales.

Typically, Nonlinear Shallow Water Equations (NSWE) are solved in conjunction with a sediment mass continuity equation. As for many phenomena influenced by multiple physical processes, coupled/uncoupled modeling of such mechanisms can lead to significant differences in predictions. In principle, it is reasonable to envisage significant differences between computations where the hydrodynamics are fully-coupled, weakly-coupled or uncoupled with the morphodynamics. Recent studies discussing this problem, e.g. Zhu and Dodd (2013), show that differences between fully coupled and uncoupled approaches accumulate during a swash event, dependent on the sediment transport formula in use.

The present study aims to understand the importance of coupled/un-coupled modeling for predictions of the swash zone sediment transport and morphology. In more details, we show that for dam-break events, similar to those forcing swash uprush events, weakly-coupled and uncoupled solutions are similar far from the dam, especially for steeper beach slopes. Closer to the dam-break location, corresponding to the location of the initiation of the swash, differences are larger.

The paper is structured as follows. The second section provides a brief description of the model background, the solver framework and the model limitations. Subsequently (Section 3.1), laboratory experiments and numerical setup are illustrated. Results are detailed in Section 4, including hydrodynamic calibration of the model and comparison between measured and predicted tip celerity and sediment transport. Final conclusions close the paper.

2. Numerical model

The solver used for the numerical simulations, described in Postacchini et al. (2012), is based on the NSWE, which are depth-

* Corresponding author. Tel.: +39 071 220 4539; fax: +39 071 220 4525.
E-mail address: m.postacchini@univpm.it (M. Postacchini).

http://dx.doi.org/10.1016/j.coastaleng.2014.04.003
0378-3839/

averaged, wave-resolving equations of conservation of mass and momentum. They describe wave breaking in terms of flow discontinuities and include seabed friction. The sediment flux and bed-level changes are calculated using standard sediment transport models and the Exner equation, which represents the solid mass conservation equation. One of the difficulties in obtaining good solutions derives from the large number of closure laws that are available to describe the sediment transport.

The NSWE/Exner system, written in conservative form, is a quasi-linear, hyperbolic set of equations. Such a fully-coupled system, could be solved through the "method of characteristics", this requiring intricate and, at times, analytically unsolvable computations for finding the resulting eigenvalues (e.g., see Kelly and Dodd, 2010). Hence, our solver is based on a rather different perspective. It does not directly solve the "method of characteristics", which requires the computation of the wave structure for the entire system, rather it is built on a weakly-coupled approach, which combines the separate hydrodynamic and morphodynamic solutions. By means of a switch, the model can solve the NSWE separately from the Exner equation. This makes the solver suitable to be used as either a weakly-coupled model, which we refer to as "coupled" hereafter, or an uncoupled model. In the former case, the hydrodynamic solution represents the initial condition for the morphodynamic solution, which, in turn, is the initial condition for the hydrodynamic solution at the following time step. In the latter case, the hydrodynamics are the initial condition for the Exner equation, whose solution does not affect the following hydrodynamic solution, but is only used to find the morphodynamic solution at the following time step.

2.1. The HM solver

The hydro-morphodynamic (HM) solver is built on the NSWE/Exner system. In its non-conservative form this reads:

$$d_{,t} + (ud)_{,x} + (vd)_{,y} = 0, \tag{1}$$

$$u_{,t} + uu_{,x} + vu_{,y} + gd_{,x} = -gz_{b,x} - B_x + F_x, \tag{2}$$

$$v_{,t} + uv_{,x} + vv_{,y} + gd_{,y} = -gz_{b,y} - B_y + F_y, \tag{3}$$

$$z_{b,t} + \mu^{-1}\nabla \cdot \mathbf{q} = 0, \tag{4}$$

where (x, y, z) are Cartesian orthogonal coordinates, d the total water depth, z_b the seabed position with respect to the still-water level, $\mathbf{v} = (u, v)$ the depth-averaged velocity vector, g gravitational acceleration, $\mathbf{q} = (q_x, q_y)$ the sediment transport flux and μ the grain packing. B_x and B_y represent the seabed friction, defined using a Chezy-type formulation by means of the dimensionless coefficient C_f.

In comparison to Postacchini et al. (2012), two further terms are introduced, i.e. F_x and F_y, which are the dissipative forces induced by subgrid turbulence, i.e. that turbulence which evolves at scales smaller than the water depth. Turbulent stresses are evaluated as:

$$F_x = \frac{(dT_{xx})_{,x} + \left(dT_{xy}\right)_{,y}}{d}, \quad F_y = \frac{\left(dT_{xy}\right)_{,x} + \left(dT_{yy}\right)_{,y}}{d}, \tag{5}$$

$$T_{xx} = 2\nu_T u_{,x}, \quad T_{xy} = \nu_T\left(u_{,y} + v_{,y}\right), \quad T_{yy} = 2\nu_T v_{,y}, \tag{6}$$

and the eddy viscosity is modeled as:

$$\nu_T = \lambda g^{1/2} d^{3/2}, \tag{7}$$

where λ is a calibration factor, similar to that adopted by van Prooijen et al. (2005).

An operational-split solution of the NSWE/Exner system is achieved by separately solving the NSWE and the Exner equation. The former is solved using the Weighted Average Flux (WAF) method, described in Brocchini et al. (2001), which has also been applied for the solution of the Exner equation. Further details on the solution of both the NSWE and Exner equation and the procedure used for their coupling can be found in Postacchini et al. (2012).

The morphodynamic module has been developed to properly match the hydrodynamic solver, which provides the forcing to update (4) in time. Uncoupled models are often characterized by the use of different approaches to solve the system at hand; Postacchini et al., (2012) decided to be consistent with the numerical scheme used for the hydrodynamic solver, thus choosing a finite-volume method for the Exner equation.

The solver enables the user to choose among different types of sediment transport closure laws, the total sediment transport ($\mathbf{q}$) being computed as the sum of both bedload ($\mathbf{q}_b$) and suspended ($\mathbf{q}_s$) contributions. Due to the weakly-coupled approach, both simple and complex closures that are available in the literature can be used in the solver (e.g. Grass, 1981; van Rijn, 1984). Implementation of these formulae requires the evaluation of the transport coefficients which are contained in the various formulations.

Since the present study is only aimed at comparing the solid transport predicted by the model with available total load measurements, the suspended sediment contribution is deactivated, while the modified Meyer–Peter–Müller formula (see Besio et al., 2003) is used for the total load description:

$$\mathbf{q} = C\sqrt{(s-1)gd_{50}^3}\left(|\boldsymbol{\theta} - \gamma\nabla z_b| - \theta_c\right)^{\frac{3}{2}} \frac{\boldsymbol{\theta} - \gamma\nabla z_b}{|\boldsymbol{\theta} - \gamma\nabla z_b|}, \tag{8}$$

where the Shields parameter for the incipient sediment motion is defined as

$$\boldsymbol{\theta} = \frac{C_f \mathbf{v}^2}{(s-1)gd_{50}}. \tag{9}$$

Closure (8) accounts for the water (ρ) and sediment (ρ_s) density through $s = \rho_s/\rho$, the median sediment diameter (d_{50}), the critical Shields parameter ($\theta_c = 0.05$), the stabilizing effect of gravity ($\gamma = 0.1$, as suggested by Fredsøe (1974)) and the spatial bed level variation estimated (∇z_b), which is computed at the grid scale. The transport coefficient used by Besio et al. (2003) is $C = 8$, but it is here set to 12, in agreement with the observations discussed in the coastal literature (e.g. Baldock et al., 2005; Nielsen, 1992).

2.2. Model limitations

Similarly to the majority of hydro-morphodynamics models (e.g. Zhu and Dodd, 2013), a constant friction coefficient is used, this providing an important constraint for the hydrodynamic calibration. There is considerable discussion on the value of the friction factor to be used during uprush and backwash and how the friction should be incorporated into models (e.g. Puleo et al., 2012). The simplest approach is to use a single value for the uprush and backwash, this depending on both the hydrodynamics and the grain size. Additionally, for swash zone flows the friction factor should be in the range $f_w = 2C_f = 0.01 - 0.05$ for a grain size $d_{50} = 0.2$ mm (Baldock et al., 2005), but not much is known on the range of the friction value for coarser materials (see Othman et al., 2014, for recent measurements and modeling). Nevertheless, the value of friction factor does not necessarily relate to the physical value of the actual friction factor, which is also hard to determine accurately for unsteady flows (e.g., see Barnes et al., 2009).

2.3. Coupled and uncoupled morphodynamics

Before comparing the coupled/uncoupled model results with the laboratory experiments described in Section 3, the morphodynamics induced by two different versions of the HM solver are analyzed and compared. For this purpose, two of the numerical simulations illustrated in Postacchini et al. (2012), run using the weakly-coupled model, are recalled. The same simulations have been re-run using the uncoupled approach.

We illustrate the exact Riemann solution of a dam-break event and one experimental/numerical test, called the Louvain test (see Fraccarollo and Capart, 2002, hereinafter FC02). The exact Riemann solution has been reproduced using the closure law $\mathbf{q} = A_d d\mathbf{v}|\mathbf{v}|^2$, while for the experiment of FC02 we used $\mathbf{q} = A\mathbf{v}|\mathbf{v}|^2$, where A_d and A are constants depending on the sediment characteristics. The differences with respect to Postacchini et al. (2012) are: i) the mesh size used in the Riemann tests, which now is $(\Delta x, \Delta y) = (0.02, 0.1)$ m and ii) the use of both coupled and uncoupled tests.

The tests can be characterized either by a mobility number $\Psi = \frac{U_0^2}{(s-1)gd_{50}}$ (e.g. Roos and Blondeaux, 2001), where we take U_0 as the flow velocity at the bore tip, or, as derived by Briganti et al. (2012), by the parameter $A = \frac{8C_f^{3/2}}{(s-1)g}$. The Riemann test can be characterized by A, which is estimated as $A = A_d d = 0.004\ \mathrm{s^2 m^{-1}}$. The Louvain test can be identified by both $A = (0.0025 - 0.004)\ \mathrm{s^2 m^{-1}}$ and $\Psi \cong 40$.

Fig. 1 illustrates the free-surface level (top panel) and the bed evolution (bottom panel) of the exact Riemann solution (gray solid lines), the coupled HM solver (thick solid lines) and the uncoupled HM solver (thick dashed lines). The maximum erosion, after 5 s of simulation, occurs around $x = 0$, where differences between the exact and the coupled solutions are negligible, while the uncoupled solution shows large discrepancies with an erosion which is about 2.5 times larger than that of the exact solution and concentrated at $x = 0$. Significant differences between the uncoupled and coupled/exact solutions are also visible in the comparison of the water surfaces. For $x < -5$ m and $x > 5$ m the coupled and uncoupled results closely reproduce the exact solution in terms of both bed changes and water level.

In Fig. 2, which shows the free-surface level, the liquid-granular mixture boundary and the bed evolution of the Louvain test, experimental data and theoretical solutions found using the three-layer model of FC02 are compared with the coupled (thick solid lines) and uncoupled (thick dashed lines) results of the HM model. After 1 s, the coupled results, over all the domain, are very close to both the theoretical solutions

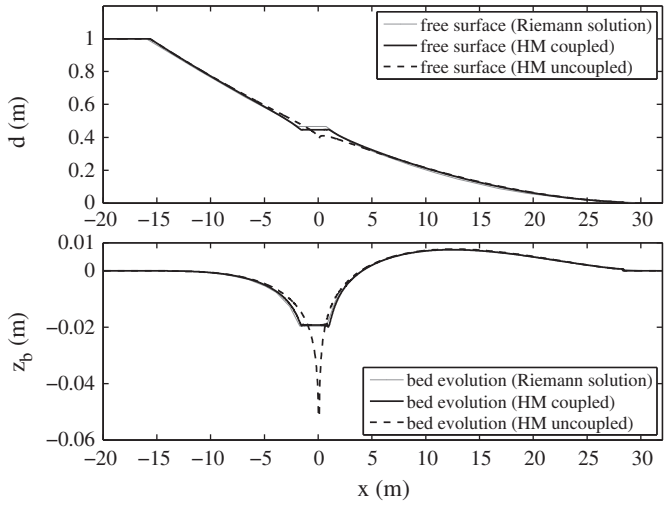

Fig. 1. Exact Riemann solution (gray solid lines) compared with coupled (black solid lines) and uncoupled (black dashed lines) results of the HM solver: free surface (top panel) and bed evolution (bottom panel) at $t = 5$ s.

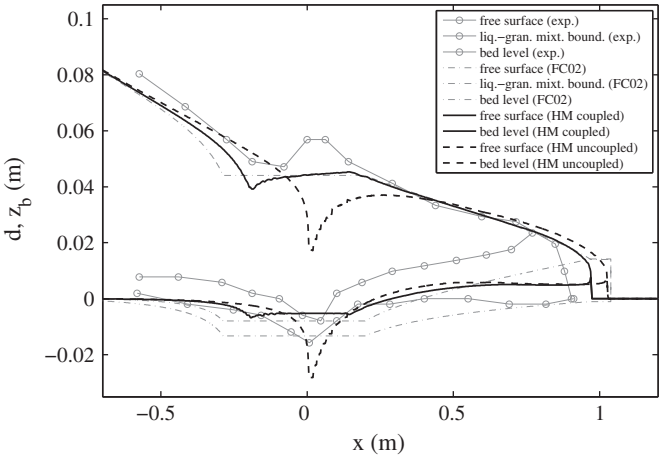

Fig. 2. Experimental data (gray solid lines and circles) and theoretical solutions (gray dash-dotted lines) of the Louvain test (FC02) compared with coupled (black solid lines) and uncoupled (black dashed lines) results of the HM solver at $t = 1$ s.

and experimental data of FC02, or at least lie between them (e.g. see the tip position at $x = 0.97$ m and the scour at $z_b = -0.06$ m),in terms of both hydrodynamics and morphodynamics. The wave tip in the uncoupled model propagates faster than in both the coupled model and the experimental data, but it is close to the theoretical solution for the wave tip. On the other hand, the scour at the dam position predicted by the uncoupled model is much greater (around 4 times) than that from the coupled model, the FC02 model and the experimental observations.

To summarize such comparisons, the hydro-morphodynamics at the tip of a dam-break wave are well predicted by the uncoupled model. The free surface and bed evolution are nearly identical when we compare coupled and uncoupled results, despite the tip not propagating at the same celerity, with the difference in the position being around 0.5% and 5.4%, respectively for the Riemann and the FC02 test. At the same time, the uncoupled prediction of the erosion at the dam position is unrealistic, hence the uncoupled model cannot be taken to reproduce the hydro-morphodynamics at such a location. The bed variation at the dam location ($x = 0$) predicted by the uncoupled model is more than 2.5 (Riemann) and 5 (FC02) times larger than those predicted by the coupled models. In fact, the strong depth and velocity gradients at the dam location induce large bed level changes, which strongly influence the hydrodynamics, this suggesting that coupling is necessary to provide realistic numerical results.

3. Experimental and numerical setup

3.1. Laboratory experiments

Experiments were carried out at the Seddon Hydraulics Laboratory, University of Queensland (Australia), to simulate a swash uprush overtopping a mobile sediment bed, by using a tilting dam-break apparatus (Fig. 3). The dam break flume was previously used in a number of experiments devoted to the study of either the bed shear stress (e.g. Barnes and Baldock, 2010) or the overtopping (Hogg et al., 2011) during swash-type dam break flows over an initially dry fixed bed. The gate opening was performed manually using a pivoting arm and is effectively nearly instantaneous (Barnes et al., 2009). A similar experimental configuration has been used by Antuono et al. (2009) to analytically investigate the early stages of the flow. For the experiments at hand, a 2 cm-thick layer of sand was placed over the entire length of the downstream side of the gate. Various initial still water levels (h_0) were used in the reservoir, ranging between 10 cm and 25 cm. Experiments characterized by different grain sizes ($d_{50} = 0.22$ mm, 2.65 mm)

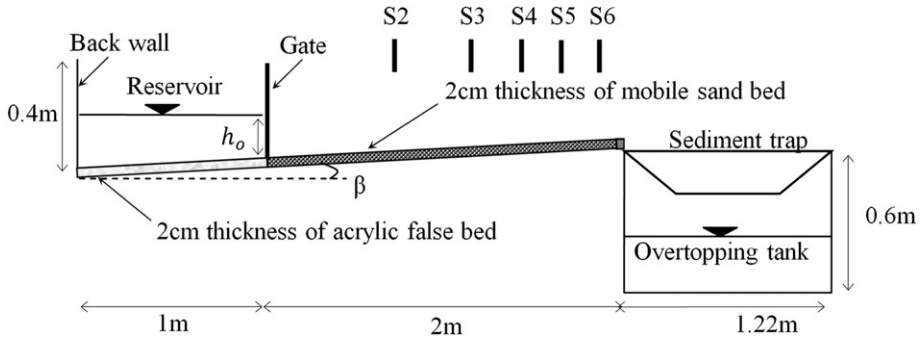

Fig. 3. Experimental setup.

and bed slopes ($tan\beta = 1/10, 1/20, 1/30, 0$) are analyzed here. The tests are characterized by the following mobility parameters: $A = 0.0014\ s^2m^{-1}$, $\Psi \cong 70 - 280$ and $A = 0.0026\ s^2m^{-1}$, $\Psi \cong 6 - 40$, respectively for fine and coarse sands.

Since it is very difficult to measure bedload and suspended load separately in such shallow and transient flows, the total transport was measured by enabling both fluid and sediment to overtop the end of the flume, where it was collected. The water depths were measured at five different locations (S2–S6) using acoustic sensors sampling at 50 Hz. The total transport Q_m is measured by trapping the overtopped sediment by means of a removable sediment trap, sitting on the overtopping tank. Further details on both facilities and experimental setup are given in Table 1, Fig. 3 and in Othman et al. (2014).

3.2. Numerical simulations

Test cases with various initial reservoir depths and different bed slopes with $d_{50} = 0.22$ mm and 2.65 mm (i.e. fine and coarse sand) have been simulated, with 21 uncoupled-model runs and 21 coupled-model runs. The "coupling switch" activates the model to:

- firstly, solve the NSWE, starting from (d, u, v) at time n and obtaining (d, u, v) at time $n + 1$,
- secondly, solve the Exner equation by means of (d, u, v) at time $n + 1$ and z_b at time n, thus obtaining z_b at time $n + 1$,
- then restart the loop with all the updated values found at time $n + 1$.

If the switch is deactivated, the updated bed does not affect the hydrodynamics, but only the solution of the Exner equation at the following loop.

The numerical domain is rectangular in the horizontal plane and coordinates x and y are used to span the plane of interest. To properly reproduce the experimental setup and the dam-break event, the total width is 0.4 m (along y), the total length 4 m (along x) and the spatial discretization $(\Delta x, \Delta y) = (0.005, 0.05)$ m. In order to assess the influence of the grid size on the solution, numerical simulations with a refined numerical grid, in the y direction, have been carried out, these leading to an almost identical hydrodynamics. As an example, when $\Delta y = 0.005$ m the tip position and the tip depth change, respectively, by about 0.1% and 0.2%.

Table 1
Test configurations.

d_{50} (mm)	$tan\beta$	h_0 (m)	d_{50} (mm)	$tan\beta$	h_0 (m)
0.22	1/10	0.22, 0.23, 0.24, 0.25	2.65	1/10	0.24, 0.25
	1/20	0.16, 0.18, 0.20		1/20	0.18, 0.20
	1/30	0.14, 0.16, 0.18		1/30	0.16, 0.18
	0	0.10, 0.12, 0.14		0	0.14, 0.16

Free fall into the overtopping tank occurs at $x = 3$ m. A mobile bed characterizes the region downstream of the gate, and a rigid bed is specified in the reservoir area upstream of the gate, similar to the experimental setup described in 3.1.

Each run is characterized by a duration of 10 s. Time series of water surface elevation (η) and velocity ($\mathbf{v}$) are determined from the model at each experimental sensor location.

4. Results

We describe the main findings related to both the capability of the HM solver in simulating the laboratory experiments and the differences between the results from the coupled and the uncoupled versions of the model. First, a hydrodynamic calibration, needed to find the values of C_f and λ that give the best match between experimental data and numerical results, has been performed. Then, the wave tip velocity and total sediment transport are evaluated for both the experiments and numerical simulations.

4.1. Hydrodynamic calibration

The hydrodynamic calibration is conducted by comparing the measured water depth (d_m) with that predicted by the coupled model

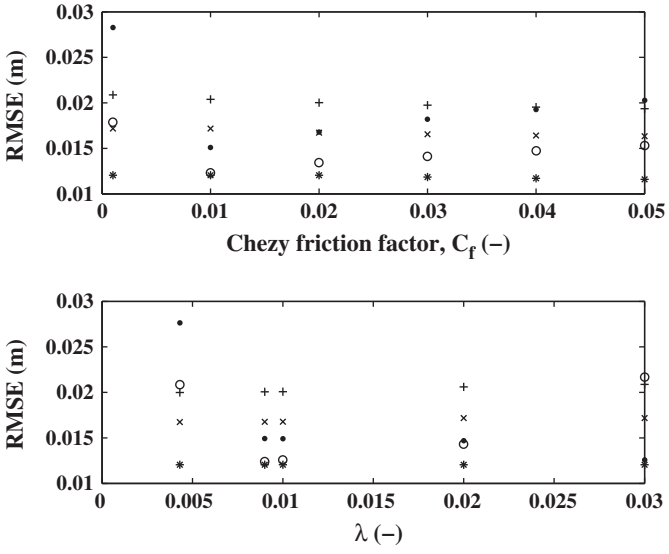

Fig. 4. RMSE of Chezy friction factor C_f (top) and viscous coefficient λ (bottom) for $h_0 = 25$ cm, $d_{50} = 0.22$ mm and $tan\beta = 1/10$; sensor locations with respect to back wall are $x = 1.535$ m (S2, ·), $x = 2.235$ m (S3, ○), $x = 2.635$ m (S4, +), $x = 2.775$ m (S5, ×) and $x = 2.955$ m (S6, ∗).

at every sensor location (d_p). Tests with several values of C_f and λ were performed, with the aim to minimize the root mean square error (RMSE) between measurement and model. Fig. 4 shows the RMSE results for a test with $h_0 = 25$ cm, $tan\beta = 1/10$ and $d_{50} = 0.22$ mm.

The best compromise among all the sensors can be achieved taking $C_f = 0.02$, for tests with $d_{50} = 0.22$ mm, and $C_f = 0.03$, for tests with $d_{50} = 2.65$ mm. The viscous contribution for each test is best accounted for by taking $\lambda = 0.009$.

Examples of the comparison between experimental data (crosses) and the coupled (solid lines) and uncoupled (dashed lines) results for depth and horizontal velocity are given in Fig. 5, at locations corresponding to the sensors located closest to the overtopping edge (S5 and S6). The predicted depths show a steeper bore and faster bore propagation (less diffusive bore) that leads the measurements, with the maximum predicted depth for the uncoupled model slightly larger than for the coupled model. The slower rise in the measured depth is due to the mobile bed that slows down the tip propagation. Such an effect is due to the erodible bed and not captured by the model. Further, the difference between the coupled and uncoupled model in terms of predicted flow velocity is negligible, except that the former leads to a longer overtopping duration. The difference between the measured and numerically predicted hydrodynamics can arise partly from infiltration effects and other small-scale processes, such as surface tension and two-phase flow (mixture of sand-water) effects, which are not taken into account in the model. Both measured (circles) and predicted (triangles) tip celerities are about 25 − 30 % larger than the numerical peak velocity, here added only as a reference velocity.

Indeed, in general, the maximum predicted flow velocity by depth-averaged models is significantly different from the tip celerity (e.g., see Barnes and Baldock, 2010; Barnes et al., 2009), but analytical computations can provide a better estimate. As suggested by Brocchini et al. (2001) (eq. 4.36), the shoreline motion $u_s = \frac{dx_s}{dt}$ during a dam-break event, which can be seen as the predicted tip celerity c_p, can be estimated from two terms on the wet side of the shoreline, i.e. the flow velocity u_p and the wave celerity, which, in the shallow water framework, is $\sqrt{gh_p}$:

$$c_p = u_p + 2\sqrt{gh_p}. \tag{10}$$

An example is shown in Fig. 6, where the predicted tip celerity (triangle) is 30% larger than the maximum flow velocity (asterisk), which is consistent with Fig. 5.

In summary, both coupled and uncoupled models predict fairly well the variation of water depth (the time lag of the maximum depth is less than 10% of the total duration), the maximum flow depth (variations smaller than 5%) and the flow velocity (as illustrated in Fig. 6). More quantitative details on the comparison between numerical and measured tip celerities are presented in the next section.

4.2. Influence on the tip celerity

Fig. 7 illustrates that the differences in the predicted tip celerity between the coupled and uncoupled runs are small, especially for the milder bed slopes (see top panel that shows the results for $tan\beta = 0$). For the case with $tan\beta = 1/10$ (bottom panel), the sensor close to the gate ($x = 1.535$ m from back wall) shows the maximum difference between coupled and uncoupled results (around 4%), while the downstream-located sensors show a difference of 2% or less. The discrepancies become insignificant for a horizontal bed, with a maximum difference of 2% for the sensor close to the gate, and 1% or less for other sensors.

The findings in Fig. 7 are not in conflict with those by Zhu and Dodd (2013). They found that differences between uncoupled and coupled approaches accumulate during an entire swash event (i.e. also accounting for the backwash phase) and uncoupled solutions tend to overestimate both velocity and sediment flux (see figure 7 of Zhu and Dodd,

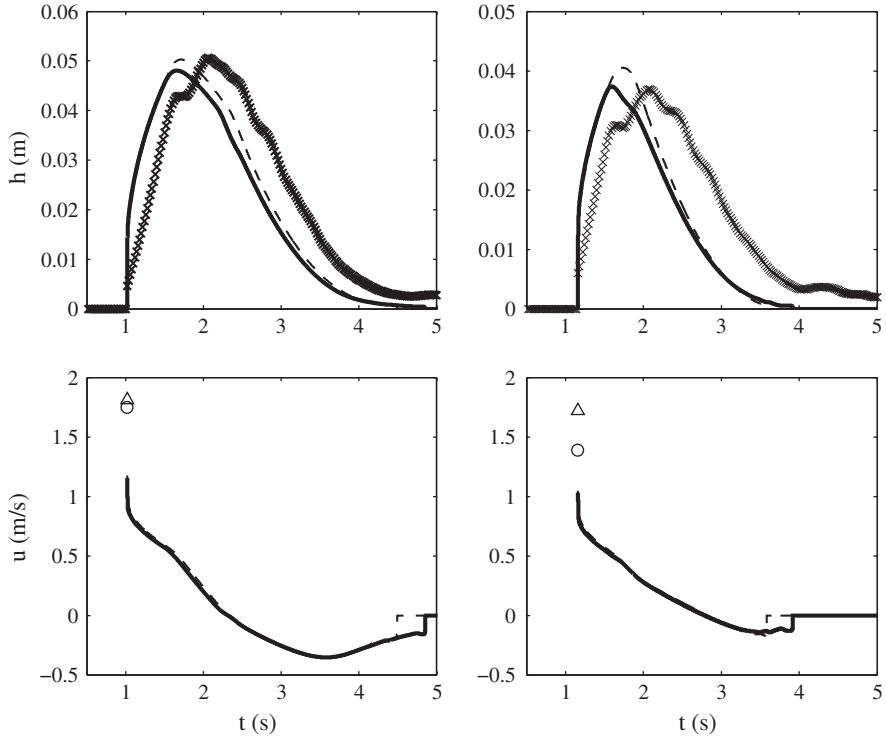

Fig. 5. Total flow depth d (top), and depth-averaged horizontal velocity u (bottom), at $x = 2.775$ m (left) and $x = 2.955$ m (right) for $d_{50} = 0.22$ mm; results coming from data (×), uncoupled (dashed line) and coupled (solid line) runs; measured (○) and predicted (△) tip celerities.

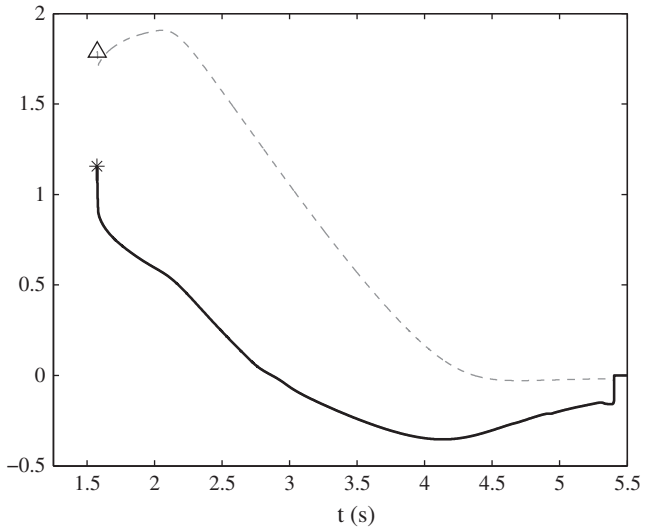

Fig. 6. Estimate of the predicted tip celerity: velocity (solid line), celerity (dashed line), maximum velocity (∗), tip celerity (△).

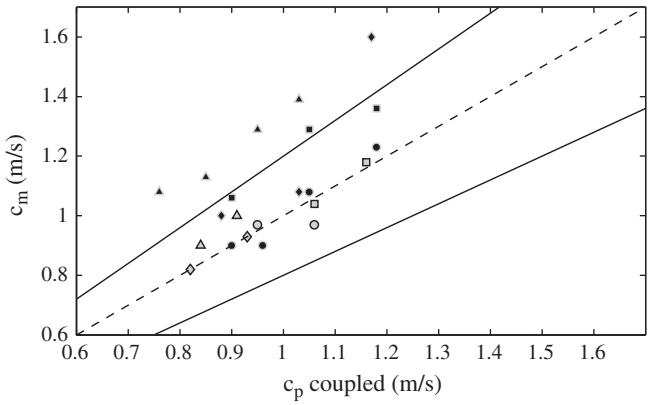

Fig. 8. Measured and predicted (coupled model) wave tip celerities with $d_{50} = 0.22$ mm (black) and $d_{50} = 2.65$ mm (gray) for slopes: $tan\beta = 1/10$ (△), 1/20 (◊), 1/30 (○) and 0 (□) at $x = 2.955$ m from the back wall. Dashed line is the bisector, while solid lines represent ± 20 % error bands.

2013), during both backwash and uprush. This is also confirmed by Fig. 7, especially for $c_p > 1.3$ m/s.

It is expected that the sediment transport calculated using either the coupled or uncoupled model will not give substantial variation since the present experiments involve only a small bed evolution, except close to the gate, with the velocity prediction at the overtopping edge being less affected by the morphological changes. Since the total sediment transport is calculated using the velocity at the overtopping edge, it is of interest to compare the tip celerity predicted by the coupled model and that measured at the overtopping edge. Most of the predicted tip celerities underestimate the measurement, but are within a ±20% error band, except for the steepest bed slope which is underpredicted by about 30% (see Fig. 8).

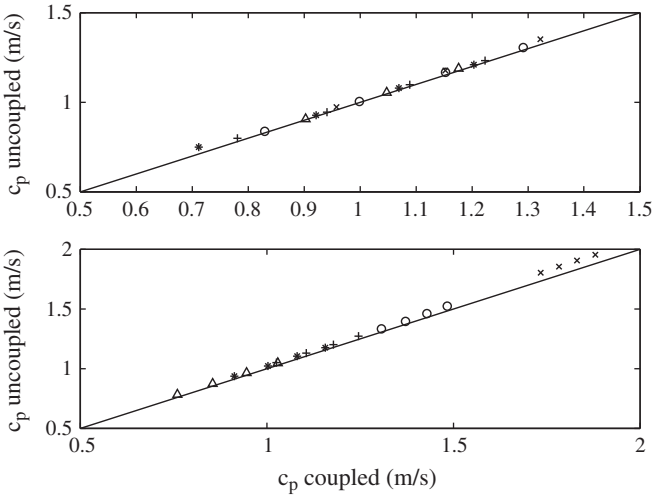

Fig. 7. Wave tip celerity for coupled and uncoupled simulations, with $d_{50} = 0.22$ mm, $tan\beta = 0$ (top) and $tan\beta = 1/10$ (bottom); results have been taken at $x = 1.535$ m (×), $x = 2.235$ m (○), $x = 2.635$ m (+), $x = 2.775$ m (∗) and $x = 2.955$ m (△) from the back wall.

4.3. Total sediment transport prediction

The predicted total sediment transport ($Q_p = \int q_x dt$) near the overtopping edge, i.e. at $x = 2.955$ m from the back wall, is compared with the sand trap measurements. The comparison takes into account only the uprush of a single bore, i.e. when the cross-shore velocities are positive.

Similar to the comparison illustrated in Fig. 7, we show here how coupling behaves in the case of the sediment transport description. Fig. 9 illustrates that, at the overtopping edge, very small differences occur between coupled and uncoupled results, i.e. around 11%.

The model predictions are compared with the measurements (Fig. 10). A reasonably close agreement is found between measured and predicted total transport, with $Q_m = 1.3\ Q_p$ for fine sand and $Q_m = 0.63\ Q_p$ for coarse sand, using standard model coefficients, with very high correlation between model and measurements. Although the predictions are within a factor 2 of the measurements, the vertical offset at small transport rates suggests however that the threshold of motion is not well described by $\theta_c = 0.05$, and that a smaller value could be more appropriate. Further, the different gradient between the best fit lines for the fine sand and coarse sand shows that the grain size variation is not fully captured by the sediment transport model. Othman et al. (2014) present a more detailed analysis of the

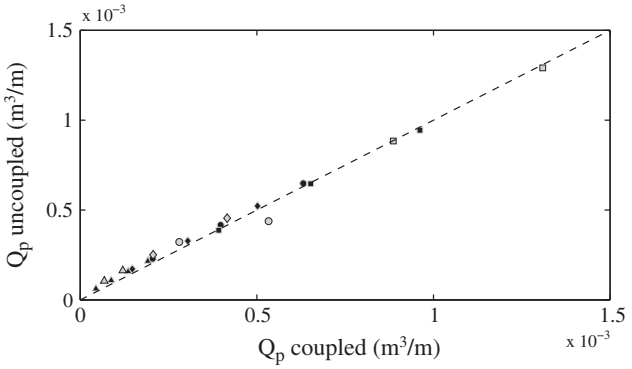

Fig. 9. Total predicted sediment transport for coupled and uncoupled simulations, with $d_{50} = 0.22$ mm (black) and $d_{50} = 2.65$ mm (gray) for slopes $tan\beta = 1/10$ (△), 1/20 (◊), 1/30 (○) and 0 (□).

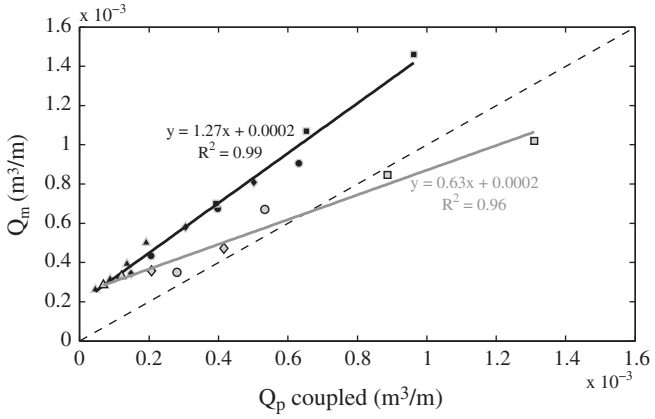

Fig. 10. Total measured (Q_m) versus predicted (Q_p) sediment transport, for $d_{50} = 0.22$ mm (black) and $d_{50} = 2.65$ mm (gray) and for $tan\beta = 1/10$ (△), 1/20 (◊), 1/30 (○), 0 (□). Solid lines represent the best fit for fine-sand (black) and coarse-sand (gray) data.

influence of grain size on the sediment transport rates for a range of different forcing parameters and sediment transport models.

5. Conclusions

Laboratory dam-break tests have been reproduced numerically by using the hydro-morphodynamic solver of Postacchini et al. (2012), built on the depth-averaged Nonlinear Shallow Water Equations (NSWE) and on the Exner mass conservation equation. A closure law for the sediment transport description can be chosen among a large variety: for this purpose, the numerical model "weakly" couples hydrodynamics and morphodynamics, i.e. the NSWE and the Exner equation are not solved simultaneously, but are updated after each time step.

We have evaluated the skill of the model in correctly predicting the experimental data and, since the solver enables both coupled and uncoupled simulations, we have also analyzed the role played by the numerical coupling on the sediment transport due to a dam-break event.

The comparisons between laboratory data and numerical results show that the hydrodynamics are well predicted, i.e. a variation of around 10% and 5%, respectively, for the timing and the value of the maximum flow depth. Such results have also been used for calibrating the friction factor and the eddy viscosity of the subgrid turbulence model. Further, comparisons of the hydro-morphodynamics reveal a fairly good agreement between experimental data and numerical prediction, i.e. the majority of the data are within a ±20% error band (tip celerity) or are characterized by a mean error around 40% (sediment transport).

No evident differences have been found between coupled and uncoupled runs, suggesting that for the special case analyzed here, i.e. the uprush phase of a swash event, the hydro-morphological coupling is not an issue of fundamental importance. However, previous comparisons between coupled, weakly-coupled and uncoupled models show that in some regimes, e.g. after a complete swash event, as presented in Postacchini et al. (2012), the uncoupled approach is significantly different from the correct solution, while the weakly-coupled one is better, though it still does not fully reproduce the fully-coupled result.

Further, the present work shows how both the weakly-coupled and uncoupled approaches are appropriate for describing the hydrodynamics and the morphodynamics during dam-break wave propagation, especially at the tip, where they provide very similar results of water-level and bed-evolution, while the difference in the tip position is smaller than 6%. On the contrary, the uncoupled model is not appropriate for predicting the hydro-morphodynamics in the region close to the dam release (errors larger than 100%), where the largest erosion occurs.

Acknowledgements

The authors acknowledge the financial support by: 1) the Italian RITMARE Flagship Project, a National Research Programme funded by the Italian Ministry of University and Research, 2) the EC FP7 Marie Curie Actions People, Contract PIRSES-GA-2011-295162 — ENVICOP project (Environmentally Friendly Coastal Protection in a Changing Climate), 3) the US-ONR, through the NICOP Research Grant (N62909-13-1-N020), 4) the Australian Research Council through project DP110101176, and 5) the Ministry of Higher Education Malaysia through a scholarship to Ilya Othman.

References

Aagaard, T., Hughes, M.G., 2006. Sediment suspension and turbulence in the swash zone of dissipative beaches. Mar. Geol. 228, 117–135.
Alsina, J.M., Cáceres, I., Brocchini, M., Baldock, T., 2012. An experimental study on sediment transport and bed evolution under different swash zone morphological conditions. Coast. Eng. 68, 31–43.
Antuono, M., Hogg, A.J., Brocchini, M., 2009. The early stages of shallow flows in an inclined flume. J. Fluid Mech. 633, 285–309.
Bakhtyar, R., Barry, D.A., Yeganeh-Bakhtiary, A., Parlange, J.-Y., Sander, G.C., 2010. Numerical simulation of two-phase flow for sediment transport in the inner-surf and swash zones. Adv. Water Resour. 33, 277–290.
Baldock, T.E., Hughes, M.G., Day, K., Louys, J., 2005. Swash overtopping and sediment overwash on a truncated beach. Coast. Eng. 52 (7), 633–645.
Baldock, T., Alsina, J.M., Cáceres, I., Vicinanza, D., Contestabile, P., Power, H., Sánchez-Arcilla, A., 2011. Large-scale experiments on beach profile evolution and surf and swash zone sediment transport induced by long waves, wave groups and random waves. Coast. Eng. 58, 214–227.
Barnes, M.P., Baldock, T.E., 2010. A lagrangian model for boundary layer growth and bed shear stress in the swash zone. Coast. Eng. 57 (4), 385–396.
Barnes, M.P., O'Donoghue, T., Alsina, J.M., Baldock, T.E., 2009. Direct bed shear stress measurements in bore-driven swash. Coast. Eng. 56 (8), 853–867.
Besio, G., Blondeaux, P., Frisina, P., 2003. A note on tidally generated sand waves. J. Fluid Mech. 485, 171–190.
Blenkinsopp, C.E., Turner, I.L., Masselink, G., Russell, P.E., 2011. Swash zone sediment fluxes: field observations. Coast. Eng. 58, 28–44.
Briganti, R., Dodd, N., Kelly, D., Pokrajac, D., 2012. An efficient and flexible solver for the simulation of the morphodynamics of fast evolving flows on coarse sediment beaches. Int. J. Numer. Methods Fluids 69, 859–877.
Brocchini, M., 2013. Bore-generated macrovortices on erodible beds. J. Fluid Mech. 734, 486–508.
Brocchini, M., Baldock, T., 2008. Recent advances in modeling swash zone dynamics: influence of surf-swash interaction on nearshore hydrodynamics and morphodynamics. Rev. Geophys. 46, 1–21.
Brocchini, M., Bernetti, R., Mancinelli, A., Albertini, G., 2001. An efficient solver for nearshore flows based on the WAF method. Coast. Eng. 43, 105–129.
Elfrink, B., Baldock, T., 2002. Hydrodynamics and sediment transport in the swash zone: a review and perspectives. Coast. Eng. 45, 149–167.
Fraccarollo, L., Capart, H., 2002. Riemann wave description of erosional dam-break flows. J. Fluid Mech. 461, 183–228.
Fredsøe, J., 1974. On the development of dunes in erodible channels. J. Fluid Mech. 64, 1–16.
Grass, A.J., 1981. Sediment Transport by Waves and Currents. SERC, London.
Hogg, A.J., Baldock, T.E., Pritchard, D., 2011. Overtopping a truncated planar beach. J. Fluid Mech. 666, 521–553.
Kelly, D.M., Dodd, N., 2010. Beach face evolution in the swash zone. J. Fluid Mech. 661, 316–340.
Masselink, G., Puleo, J.A., 2006. Swash-zone morphodynamics. Cont. Shelf Res. 26, 661–680.
Masselink, G., Russel, P., 2006. Flow velocities, sediment transport and morphological change in the swash zone of two contrasting beaches. Mar. Geol. 227, 227–240.
Nielsen, P., 1992. Coastal Bottom Boundary Layers and Sediment Transport. World Scientific Pub Co Inc.
Othman, I.K., Baldock, T.E., Callaghan, D.P., 2014. Measurement and modelling of the influence of grain size and pressure gradient on swash uprush sediment transport. Coast. Eng. 83, 1–14.
Postacchini, M., Brocchini, M., Mancinelli, A., Landon, M., 2012. A multi-purpose, intra-wave, shallow water hydro-morphodynamic solver. Adv. Water Resour. 38, 13–26.
Puleo, J.A., Lanckriet, T., Wang, P., 2012. Near bed cross-shore velocity profiles, bed shear stress and friction on the foreshore of a microtidal beach. Coast. Eng. 68, 6–16.
Roos, P.C., Blondeaux, P., 2001. Sand ripples under sea waves. Part 4. Tile ripple formation. J. Fluid Mech. 447, 227–246.
van Prooijen, B.C., Battjes, J.A., Uijttewaal, W.S.J., 2005. Momentum exchange in straight uniform compound channel flow. J. Hydraul. Eng. 131 (3), 175–183.
van Rijn, L., 1984. Sediment transport, part II: suspended load transport. J. Hydraul. Div. 110 (11), 1613–1641.
Zhu, F., Dodd, N., 2013. Net beach change in the swash zone: a numerical investigation. Adv. Water Resour. 53, 12–22.